Single Domain Antibody Inhibitors Target the Coiled Coil Arms of the *Bacillus subtilis* SMC complex

Ophélie Gosselin[1], Michael Taschner[1], Lea M. Huber-Hürlimann[2], Markus A. Seeger[2] and Stephan Gruber[1]*

[1]Department of Fundamental Microbiology (DMF), Faculty of Biology and Medicine (FBM), University of Lausanne (UNIL), 1015 Lausanne, Switzerland

[2]Institute of Medical Microbiology, University of Zurich, Zürich, Switzerland

*Corresponding Author: stephan.gruber@unil.ch

Key words: Single domain antibodies, Sybodies, nanobodies, SMC complex, bacterial condensin, DNA loop extrusion, chromosome segregation

Abstract

Synthetic nanobodies—also called sybodies—have proven valuable for stabilizing conformations of purified proteins, advancing structural and functional studies for example of transmembrane protein complexes. However, their utility in modulating protein function in living cells has remained less well explored. Structural Maintenance of Chromosomes (SMC) complexes facilitate chromosome organization by DNA loop extrusion, a fundamental process in all domains of life. In this study, we target the bacterial SMC complex, Smc-ScpAB, in *Bacillus subtilis* with synthetic nanobodies, with the aim to identify key functional regions of the protein complex in a largely unbiased manner. We first isolate sybodies that specifically bind purified Smc-ScpAB and then express them in *B. subtilis* to select binders capable of disrupting Smc-ScpAB function, leading to chromosome segregation defects and cell death. Mapping and biochemical characterization show that the fourteen disruptive sybodies belong to one of three library designs, target the Smc subunit near the same coiled coil arm interface and modulate its ATPase activity in two principal ways, highlighting the mid-region of the Smc coiled coil as critical feature of the DNA folding process. These findings underscore the potential of sybodies—and, by extension, designed binders—as versatile tools for probing dynamic protein function in living cells, with potentially broad applications in cell and synthetic biology.

30 **Introduction**

31 Rapid and specific interference with protein activity and dynamics in living cells is essential for
32 studying and understanding biological mechanisms. However, current approaches—primarily based
33 on small-molecule inhibitors—remain laborious, time-consuming, and costly. The advent of
34 conformation-specific synthetic nanobody (sybody) selection (I. Zimmermann *et al.*, 2018), and more
35 recently, computational design of protein binders (Pacesa *et al.*, 2025), offer unique opportunities for
36 protein-based inhibition and modulation of cellular targets. Here, we generate sybodies against the
37 SMC complex in *B. subtilis* to efficiently inhibit its function within cells.

38 Structural Maintenance of Chromosomes (SMC) complexes are multi-subunit, ring-shaped ATP-
39 hydrolyzing DNA motors that structure chromosomal DNA by loop extrusion. They are essential for
40 chromosome organization and segregation, gene expression, DNA repair, and defense against non-
41 self DNA across all domains of life loop (Yatskevich, Rhodes and Nasmyth, 2019). Each SMC protein
42 (Smc in *B. subtilis, bsu*Smc) is a long polypeptide with its N- and C-termini folding together to form a
43 globular ATP binding cassette (ABC) "head" domain. The head is connected to a "hinge" dimerization
44 domain via a ~50 nm antiparallel coiled coil "arm", creating an elongated dimer (Figure 1Aii and 1Aiii).
45 ATP binding promotes head engagement, bringing the heads together to form a functional ATPase.
46 Non-SMC subunits, a kleisin (ScpA in *B. subtilis*) and a dimer of KITE (ScpB in *B. subtilis*) or two HAWK
47 proteins, bridge the heads, together forming a ring around DNA (Figure 1Aiii). In *B. subtilis*, Smc-
48 ScpAB is recruited to the origin of replication (*oriC*) region on the chromosome by ParB, a DNA-
49 binding protein that recognizes centromere-like *parS* sequences (Figure 2A). Once loaded, Smc-ScpAB
50 translocates at a rate of ~1 kb/s onto flanking DNA, aligning the two chromosome arms and
51 individualizing nascent sister chromosomes (Gruber *et al.*, 2014; Bürmann and Gruber, 2015; Wang *et*
52 *al.*, 2017), likely bypassing obstacles on the chromosome through the SMC hinge gate (Liu *et al.*,
53 2025). Null mutants of *smc*, *scpA*, or *scpB* fail to segregate chromosomes properly and lose viability

54 under conditions promoting rapid growth (Sullivan, Marquis and Rudner, 2009; Gruber *et al.*, 2014;
55 Wang *et al.*, 2014).

56 Several models have been proposed for the mechanism of DNA loop extrusion by SMC complexes,
57 including the "segment capture" model, in which DNA segments are transiently trapped between the
58 SMC arms in partially open states and fused into larger loops through iterative ATP-driven cycles
59 (Figure 1Aiii and S1B) (Minnen *et al.*, 2016; Diebold-Durand *et al.*, 2017; Marko *et al.*, 2019).
60 However, detailed structural understanding and experimental testing *in vivo* are lacking.

61 Antibodies can block biochemical reactions by stabilizing reaction intermediates. Synthetic single-
62 domain antibodies called sybodies are small, robust antigen-binding proteins that were engineered
63 based on three camelid nanobody structures (I. Zimmermann *et al.*, 2018). They are selected from
64 synthetic libraries that encode a wide diversity of binding surfaces and epitope shapes based on the
65 length and geometry of their CDR3 loop, allowing strong binding of diverse antigen surfaces (Figure
66 1Ai). Their small size (~15 kDa), stability, and ability to bind transient epitopes make them ideal tools
67 for targeting specific states of biomolecules (Søren G.F. Rasmussen *et al.*, 2011). Selection is carried
68 out using purified and immobilized Smc-ScpAB by ribosome display and phage display, typically
69 followed by an ELISA-based screening (I. Zimmermann *et al.*, 2018).

70 Here, we demonstrate that sybodies can be used to interfere with the function of *B. subtilis* Smc-
71 ScpAB *in vivo*. We first isolate binders that specifically target purified Smc-ScpAB *in vitro* and then
72 select those that eliminate Smc function when expressed in *B. subtilis*. Fourteen sybodies were found
73 to disrupt chromosome segregation, mimicking *smc* deletion phenotypes. Biochemical assays
74 confirmed that selected sybodies alter the ATP hydrolysis rate of Smc-ScpAB and its stimulation by
75 DNA addition, likely stabilizing otherwise rare intermediates of the conformational cycle. Mapping
76 experiments using chimeric Smc constructs revealed that most binders, unexpectedly, target the
77 coiled coil, specifically in a defined region near the Smc 4N arm-to-arm contact, highlighting the

78 potential of sybodies and designed binders, as genetic tools to identify essential functional domains

79 and underscoring the importance of coiled coil dynamics for Smc function.

80

81 **Results**

82 **Generation of *bsuS*mc-ScpAB-specific sybodies**

83 To isolate sybodies that impede the function of *B. subtilis* Smc-ScpAB complex, we first performed *in*
84 *vitro* selections with purified Smc-ScpAB under conditions favoring an ATP-bound state, using 40 bp
85 duplex DNA, and an ATPase-deficient mutant (E1118Q) of *bsuS*mc biotinylated at the hinge at residue
86 R643C for immobilization (Figure 1A and S1A) (Hirano and Hirano, 2004; Bürmann *et al.*, 2017; I.
87 Zimmermann *et al.*, 2018; Zimmermann *et al.*, 2020). Starting from three synthetic sybody libraries
88 encoding distinct epitope-binding geometries (denoted as concave, loop, convex, respectively, Figure
89 1A), we performed one round of ribosome display followed by two rounds of phage display, thereby
90 enriching sybodies that bind to ATP- and DNA-bound Smc-ScpAB (Table 1). From each library, 95
91 sybody-expressing *E. coli* clones were randomly chosen for *in vivo* characterization.

92

93 **Identification of *bsuS*mc-ScpAB-blocking sybodies through phenotypic screening in *B. subtilis***

94 Despite containing a conserved disulfide bond, some sybodies can be expressed inside cells and bind
95 their targets in the reducing environment of the cytoplasm, likely owing to their robust folding
96 (Deneka *et al.*, 2021). To assess whether the selected sybodies interfere with Smc function *in vivo*,
97 each of the 285 sybody sequences was cloned under a xylose-inducible promoter (P_{xyl}) into an *E. coli*–
98 *B. subtilis* shuttle vector and integrated at the *amyE* locus of the wild-type 1A700 strain (Figure 1B)
99 (Diebold-Durand, Bürmann and Gruber, 2019). Fourteen sybodies from the loop library failed to yield
100 transformants in the presence (but not absence) of xylose, indicating cell lethality due to sybody
101 inhibition of Smc-ScpAB (Figure 1C, S2A). These Smc-disruptive sybodies (denoted as Sb002, 003, 006,
102 010, 015, 020, 021, 031, 156, 160, 162, 169, 188, and 194, respectively) harbor fourteen distinct
103 sequences, showing the absence of duplicates (Table S1). Intriguingly, no such disruptive sybodies
104 were isolated from the concave and convex libraries (Figure S2B), suggesting that the CDR3 geometry
105 as present in the loop library is particularly effective at targeting *bsuS*mc-ScpAB. Alternatively, the

106 other libraries did not produce good binders or these sybodies were not stably expressed in *B.*
107 *subtilis*. Notably, tendencies of preferential isolation of binders from one of the three libraries have
108 previously been observed, although at milder levels (I. Zimmermann *et al.*, 2018; Hutter *et al.*, 2019;
109 Deneka *et al.*, 2021).

110

111 **Selected sybodies target *bsuS*mc-ScpAB function *in vivo***

112 To determine whether the fourteen sybodies indeed impair chromosome segregation, we used
113 fluorescence microscopy to monitor *oriC* positioning in a *B. subtilis* strain expressing a ParB-GFP
114 fusion protein together with a P_{xyl}-inducible sybody gene. In these strains, ParB-GFP marks the
115 replication origin region by binding to *parS* sites near *oriC* (Figure 2Ai). As expected, the *Δsmc* strain
116 displayed fewer ParB-GFP foci and elongated cells, consistent with delayed *oriC* separation (Figure
117 2Ai) (Table S2) (Gruber *et al.*, 2014; Wang *et al.*, 2014). A time course experiment using sybody Sb006
118 revealed chromosome organization defects as early as 30 minutes post induction, with a significant
119 reduction in ParB-GFP foci per µm cell length at 40 minutes (p = 0.0145) (Figure 2Aii). Subsequent
120 imaging was performed ~35 minutes after induction of sybody expression.

121 All disruptive sybodies reduced ParB-GFP foci density compared to the control (1.03 foci/µm), with
122 values ranging from 0.56 foci/µm (Sb020) to 0.22 foci/µm (Sb003). These defects were all robustly
123 detected, while being less severe than the Δ*smc* mutant (~0.05 foci/µm), conceivably due to the short
124 induction time or incomplete inhibition. Milder defects were also observed without induction, likely
125 attributed to leaky expression from the P_{xyl} promoter (Figure S3A). Sybody expression also caused cell
126 elongation and growth delays, both hallmarks of impaired Smc activity, consistent with chromosome
127 segregation defects that delay cell division (Figure S3B–C). Altogether, these results show that all
128 selected sybodies induce *Δsmc*-like phenotypes likely by interfering with *bsu*Smc-ScpAB activity *in*
129 *vivo*.

130

131 **Selected sybodies specifically target *B. subtilis* Smc-ScpAB**

132 To test whether sybodies specifically target *B. subtilis* Smc-ScpAB, we assessed their effects in a strain
133 expressing *Streptococcus pneumoniae* (*Spn*) Smc-ScpAB and ParB proteins in place of the endogenous
134 *B. subtilis* proteins. The *Spn* sequences can functionally replace the corresponding *Bsu* sequences
135 despite significant sequence divergence (~38% sequence identity) (Bock *et al.*, 2022). Strikingly, none
136 of the sybodies impaired growth in this background, even though a cognate ParAB pair is absent in
137 this strain (*S. pneumoniae* lacks *parA*), sensitizing cells to chromosome segregation defects (Figure
138 2C). These results confirm that the sybodies are specific to *bsu*Smc-ScpAB and that off-target toxicity
139 is not noticeable.

140

141 ***bsuS*mc-ScpAB-disrupting sybodies target two distinct coiled coil regions adjacent to the *bsuS*mc 4N**
142 **arm-to-arm contact**

143 To map the sybody-binding site on the *bsuS*mc-ScpAB complex, we utilized five chimeric Smc
144 constructs (Smc Chimera 1-5), in which the hinge and progressively longer segments of the adjacent
145 coiled coils were replaced with the corresponding sequences from the *S. pneumoniae* Smc protein
146 (Figure 3A). Chimeric junctions were designed to preserve coiled coil integrity based on available
147 crystal structures, coiled coil predictions by DeepCoil, and AlphaFold2 structural models (L.
148 Zimmermann *et al.*, 2018; Gabler *et al.*, 2020; Jumper *et al.*, 2021). All chimeric Smc strains retained
149 the native *B. subtilis scpA*, *scpB*, and *parB* genes and were viable under conditions promoting fast
150 growth, demonstrating proper protein folding and functioning of chimeric Smc-ScpAB complexes
151 (Figure S4A).

152 Chimeras 1 and 2, which carry the central hinge and coiled coil sequences of *Spn* origin (residues 363-
153 812 and 339-836, respectively), showed the same sybody-induced growth defects as the wild-type
154 strain, indicating that the sybodies bind further away from the hinge, within the remaining *B. subtilis*
155 portion comprising of the Smc head and the first ~230 coiled coil residues, and ScpAB (Figure 3A). By

156 contrast, Chimera 5 (residues 248–927 of *Spn* origin), supported robust growth even in the presence
157 of the *bsu*Smc-disrupting sybodies, indicating that the region comprising the heads and first ~50
158 residues of the coiled coil (including the joint) does not comprise the binding site. The binding region
159 for the sybodies is thus located on the coiled coil between residues 248 and 339 (or 836 and 927),
160 demonstrating that all fourteen sybodies bind to a central region of the coiled coil.

161 Chimera 3 (*spn*Smc residues 318-857) and chimera 4 (*spn*Smc residues 276-899) revealed two distinct
162 sybody responses. Sb003, 031, 156, 160, 162, and 169 impaired growth of both strains, mapping their
163 binding sites to *B. subtilis* residues 248-276 (and 899-927), present in chimeras 1–4 but absent in
164 chimera 5. In contrast, Sb002, 006, 010, 015, 020, 021, 188, and 194 had no impact on the viability of
165 chimera 3 or 4, suggesting they target residues 318-339/836-857 (Figure 3A, 3D).

166 In sum, these experiments mapped the binding sites of all fourteen disruptive sybodies to one of two
167 ~twenty amino acid segments in the central region of the *bsuS*mc coiled coil (Figure 3D). These
168 regions harbor relatively poorly conserved sequences but flank the 4N arm-arm contact (~at residue
169 295), previously proposed to serve as an essential structural switch between closed and open
170 conformations (Vazquez Nunez *et al.*, 2021). These results reveal that all isolated sybodies target the
171 same functional element of the Smc arms, and that interfering with this element disrupts Smc-
172 dependent chromosome organization *in vivo*.

173

174 **Smc-disrupting sybodies affect the ATPase activity in one of two ways**

175 To investigate how sybodies may influence *bsuS*mc-ScpAB, we next measured ATP hydrolysis rates
176 using purified proteins in the presence and absence of DNA. SMC ATPase activity serves as an indirect
177 readout for state transitions, including arm opening and head engagement. In absence of DNA,
178 *bsuS*mc-ScpAB hydrolyzes ATP at ~4 ATP/min/Smc (Vazquez Nunez *et al.*, 2021). DNA binding
179 stimulates ATP hydrolysis to ~9 ATP/min/Smc, presumably by DNA binding at the hinge promoting
180 arm opening and head engagement, creating a more open conformation.

181 All disruptive sybodies measurably affected the ATP hydrolysis rate of *bsuS*mc-ScpAB. Ten maintained
182 a near-basal ATPase rate even in presence of DNA (Sb002, Sb003, Sb010, Sb031, Sb156, Sb160,
183 Sb162, Sb169, Sb188, and Sb194) (Figure 3B-C and S4B). This suggests that they stabilize the complex
184 in a closed or partially closed conformation, thus hindering DNA-dependent ATPase stimulation.
185 Notably, in this group, Sb002 and Sb194 showed slightly elevated ATPase rates with DNA, hinting at a
186 mildly more flexible conformation.

187 In contrast, the other sybodies (Sb006, Sb015, Sb020, and Sb021) stimulated ATP hydrolysis in the
188 absence of DNA, with Sb006 reaching levels comparable to DNA-induced activation (~10 ATP/min).
189 This implies that these sybodies stabilize Smc-ScpAB in a more open state promoting head
190 engagement. Curiously, addition of DNA in the presence of Sb006 and Sb021 reduced—rather than
191 stimulated—ATPase activity (Figure 3B-C), suggesting that concurrent DNA and sybody binding may
192 trap the complex in a non-productive conformation, perhaps by favoring the open state excessively.
193 These findings are consistent with the idea that 4N contact region plays a critical role in arm opening
194 and ATPase stimulation.

195 Interestingly, the observed ATPase profiles correlate with distinct binding regions along the Smc arms.
196 All ATPase-stimulating sybodies (Sb006, Sb015, Sb020, Sb021) bind above the 4N contact
197 ("Opening^{UP}"), while sybodies that hinder DNA stimulation fall into two subgroups: those binding
198 above the 4N contact (Sb002, Sb010, Sb188, Sb194—"Closing^{UP}") and those binding below it (Sb003,
199 Sb031, Sb156, Sb160, Sb162, Sb169—"Closing^{DOWN}") (Figure 3D). These results indicate that the
200 sybodies perturb *bsuS*mc-ScpAB in two principal ways: either by favoring the opening of the arms or
201 by constraining the arms in a more closed state. The results highlight arm opening and closure as
202 central regulatory features of bacterial Smc-ScpAB (Soh *et al.*, 2015; Minnen *et al.*, 2016; Diebold-
203 Durand *et al.*, 2017; Vazquez Nunez, Ruiz Avila and Gruber, 2019) and confirm the key role of the 4N
204 arm contact in balancing the opening and closing of SMC arms (Vazquez Nunez *et al.*, 2021).

205

206 **Discussion**

207 Over the past three decades, sybodies and their synthetic counterparts have transformed biomedical
208 research and structural biology by enabling the targeting and stabilization of transient protein
209 conformations. Despite these advances, their application to probing protein function in living cells
210 has remained limited (Seeger *et al.*, 2012; Deneka *et al.*, 2021). Here, we expand the utility of
211 synthetic sybody selection by employing it as a tool to screen for genetic probes targeting the
212 function of selected molecular machines *in vivo*. This strategy combines the advantages of controlled
213 biochemical reconstitution with the ability to study the function of proteins in their native context.
214 Importantly, sybody selection requires no prior knowledge of vulnerable regions, providing an
215 unbiased means to interrogate protein function that is difficult to achieve through rational design.
216 Our study based on the *B. subtilis* Smc-ScpAB DNA motor as a model uncovers a central regulatory
217 region in the coiled coil arms of Smc and highlight how distinct arm conformations shape SMC
218 function in loop extrusion and chromosome segregation.

219

220 **Revealing Smc arm dynamics through synthetic binders**

221 All fourteen Smc-disrupting sybodies share the loop library design. Moreover, their Smc binding sites
222 map to the two short coiled coil segments flanking the conserved 4N arm-to-arm contact, a region
223 previously implicated in key conformational transitions during arm opening (Vazquez Nunez *et al.*,
224 2021). While the fourteen sybodies harbour different epitope binding sequences, we suspect that
225 they may all bind to the Smc dimer in an analogous manner. With the long CDR3 loops known to bind
226 narrow structural cavities (Søren G. F. Rasmussen *et al.*, 2011; Kruse *et al.*, 2013), we speculate that
227 these sybodies may intercalate between the two coiled coil arms (Figure 3D). Structural studies are
228 needed to test this hypothesis directly, however, our attempts at X-ray crystallography and electron
229 microscopy of Smc-sybody complexes have failed so far.

230 Notably, while the coiled coil dimer appears similarly structured from the elbow to the hinge
231 (Diebold-Durand 2017) (Figure 3D), no Smc-disrupting sybodies mapped to regions further away from
232 the 4N contact (Figure 3D). This indicates that opening and closure of the Smc arms might be
233 dispensable at these places, although formal testing would require isolating binders efficiently
234 targeting these regions, potentially facilitated by binder design, and expressing them in *B. subtilis*.
235 This parallels with findings with the bacterial SMC defense system Wadjet, where hinge-proximal arm
236 opening is dispensable for loop extrusion, but essential for obstacle bypass (Liu *et al.*, 2025).
237 Alternatively, these arm-to-arm contacts might be more stable and thus less likely to be interfered
238 with by sybody binding. Similarly, sybodies targeting below the 4N contact all reduce the ATPase rate
239 (or rather its DNA stimulation), indicating that artificial opening at this position may not disrupt Smc
240 function (Figure S5). Again, these hypotheses need to be tested more directly. We envision that the
241 design of protein binders may allow us to confirm these observations and further dissect the
242 underlying mechanisms.

243 This work establishes sybodies as precision tools for blocking ATP-driven machines inside bacterial
244 cells. By targeting allosteric control points in Smc, they enable mechanistic dissection of loop
245 extrusion and open new avenues for studying dynamic complexes *in vivo*. More broadly, the study
246 demonstrates how synthetic binders can trap, stabilize, or block transient conformations of active
247 chromatin-associated machines, providing a powerful means to probe their mechanisms in living
248 cells. Looking ahead, the rational design of protein binders with tailored geometry and allosteric
249 potential could allow researchers to manipulate and visualize specific conformational states with
250 even greater control and refinement, across both prokaryotic and eukaryotic organisms, while the
251 generation and *in vivo* screening of sybodies remains an attractive approach to gain unexpected
252 biological insights in an unbiased manner.

253

254 **Material and Methods**

255 ***Bacillus subtilis* strains construction and growth**

256 *B. subtilis* strains used in this study were derived from the parental strain 1A700. Allelic replacement
257 was achieved via double-crossover recombination at the endogenous *smc* locus using the natural
258 competence method described by (Bürmann *et al.*, 2013). Chromosome-integration of sybody genes
259 were performed by transforming a vector containing an *amyE h*omologous regions on each side of
260 the recombinant gene of interest, as described in (Diebold-Durand, Bürmann and Gruber, 2019).
261 Transformants were selected on ONA solid medium containing the appropriate antibiotics. Following
262 transformation, strains were purified by single colony isolation and verified through a combination of
263 marker testing, phenotype assessment, PCR, and Sanger sequencing of the *smc* locus, when
264 appropriate. For spot assays, cells were cultured to stationary phase in liquid LB medium, and 9^{-2} and
265 9^{-5} dilutions were then spotted onto solid ONA medium with chloramphenicol (5 ug/mL) and xylose
266 (0.5% w/v) when induction of the P_{xyl} promoter was required. The strains, primers and plasmids used
267 in this study are listed in Table S3, Table S4 and Table S5, respectively.

268 For viability assessment, 200 LB medium was inoculated with a 1:1000 dilution of a dense *B. subtilis*
269 culture and grown to stationary phase. The culture was then serially diluted in LB medium. From each
270 dilution (9^{-1} to 9^{-8}), 5 µL was spotted onto LB agar plates containing the appropriate antibiotic
271 selection. Plates were incubated, and viability was assessed by imaging the spots at 16- and 24-hours
272 post-incubation.

273 **Sybody selection**

274 Sybody selection was performed following the protocol by (Zimmermann *et al.*, 2020) , with
275 modifications to enrich binders specific for the ATP/DNA-stabilized "open" form of the *bsuS*mc-ScpAB
276 complex.

277 **Ribosome Display**

278 The standard WTB buffer (50 mM Tris/acetate pH7.4, 150 mM NaCl, 50 mM MgAc2) and its
279 derivatives were adjusted to 50 mM NaCl to facilitate *bsuS*mc-ScpAB binding to dsDNA. The target
280 complex was assembled by mixing 500 nM *bsuS*mc(C119S, C437S, C826S, E1118Q, R643C)-ScpAB, 2
281 mM ATP, and 5 µM 40 bp dsDNA in WTB-D-BSA buffer (WTB including 0.5% (w/v) BSA and 0.1%
282 Tween-20), incubated for 15 min at room temperature (RT). The ribosome display panning solution
283 was supplemented with 2 mM ATP and 5 µM dsDNA to maintain binding conditions. Solution panning
284 and biotinylated target capture were conducted at RT to optimize selection for the "open" complex.
285 Washing steps incorporated 2 mM ATP and 5 µm 40 bp dsDNA, while elution, reverse transcription,
286 and cDNA amplification followed the original protocol. Reverse transcribed RNA molecules were
287 quantified by qPCR.

288 **First round of phage display**

289 Phagemid libraries were cloned and electroporated into *E. coli* SS320 as previously described
290 (Zimmermann *et al.*, 2020). Phage production was performed using M13KO7 helper phage. The
291 phage display buffer (TBSM) consisted of 20 mM Tris-HCl (pH 7.4), 50 mM NaCl, and 2 mM MgCl2.
292 Target preparation involved incubating 500 nM biotinylated *bsuS*mc(C119S, C437S, C826S, E1118Q,
293 R643C)ScpAB with 2 mM ATP and 5 µM dsDNA in TBSM-BSA-D (TBSM including 0.5% (w/v) BSA and
294 0.05% Tween-20). Phages (10^{12}/ml) were incubated with the target at 50 nM for 20 min at RT before
295 immobilization on neutravidin-coated plates. Washing (with added 2 mM ATP and 5 µm 40 bp dsDNA)
296 and elution otherwise followed the original protocol, with enrichment assessed by qPCR. Amplified
297 phages were used for a second selection round.

298 **Second round of phage display**

299 Purified phages from the first round were used at 5×10^{13} phages/ml, and the target was prepared as
300 in the first round. Phage-target binding occurred at 50 nM in the presence of ATP and dsDNA,
301 followed by capture on magnetic beads. A competition step using non-biotinylated *bsuS*mc-ScpAB (1
302 µM) was included before washes with TBSM-D. Phages were eluted and enrichment was determined

303 by qPCR. Phagemids were purified, sub-cloned into the pNb_init vector, and transformed into *E. coli*
304 MC1061.

305 **Growth curve analyses**

306 Growth curves were generated from *B. subtilis* strains grown overnight to exponential phase in LB
307 medium supplemented with 0.5% glucose, incubated at 30°C with shaking. The following day, fresh 5
308 mL LB cultures were inoculated with the overnight culture to an OD of 0.005 and incubated at 37°C
309 with shaking until reaching an optical density (OD) of 0.05. Subsequently, each culture was subjected
310 to a twofold dilution in a 96-well plate (Costar #3596), achieving a final volume of 200 µL per well.
311 Where necessary, cultures were induced with 0.5% xylose. Plates were incubated at 37°C with
312 continuous shaking in a Thermo Scientific Multiskan FC plate reader. Growth curves were determined
313 by light scattering at 620 nm. The BactEXTRACT app was used to perform Analysis and visualization of
314 the data (Dénéréaz and Veening, 2024).

315 **Protein purification**

316 **Purification of *bsuS*mc and biotinylated *bsuS*mc(C119S, C437S, C826S, E1118Q, R643C)**

317 *bsuS*mc proteins were purified according to (Bürmann *et al.*, 2017). pET-22 or pET-28 plasmids
318 encoding the *Smc* recombinant sequences were transformed into *E. coli* BL21-Gold (DE3) cells.
319 Protein expression was carried out in ZYM-5052 autoinduction medium for 23 hours at 24°C. The cells
320 were harvested and resuspended in lysis buffer (50 mM Tris-HCl, pH 7.5, 150 mM NaCl, 1 mM EDTA, 1
321 mM DTT, 10% (w/v) sucrose) supplemented with protease inhibitor cocktail. Cell lysis was achieved by
322 sonication, and the lysate was clarified by centrifugation. The supernatant was filtered through a 0.45
323 µm membrane and loaded onto two HiTrap Blue HP 5 mL columns connected in series. Elution was
324 performed using lysis buffer with 1 M NaCl. The main peak fractions were pooled and diluted with
325 salt-free buffer (50 mM Tris-HCl, pH 7.5; 1 mM EDTA; 1 mM DTT) to a final conductivity equivalent to
326 50 mM NaCl (~8 mS/cm). This diluted sample, supplemented with protease inhibitor cocktail, was
327 applied to a HiTrap Heparin HP 5 mL column, and the proteins were eluted using a linear gradient up

328 to 2 M NaCl. The main peak fractions (~ 5 mL) were collected and subjected to further purification by
329 gel filtration using an XK 16/70 Superose 6 PG column equilibrated with 50 mM Tris-HCl, pH 7.5, 200
330 mM NaCl, 1 mM EDTA, and 1 mM TCEP. The peak fractions were collected, concentrated using a
331 Vivaspin 15 10K MWCO filter, flash frozen in liquid nitrogen, and stored at -80°C. Protein
332 concentration was determined by absorbance, utilizing theoretical molar absorption and molecular
333 weight values.

334 For the biotinylated *bsu*Smc(C119S, C437S, C826S, E1118Q, R643C) protein used in the sybody
335 selection, the protein was first purified as described above, except that the reducing agent (TCEP) was
336 omitted from the final gel filtration buffer. Labelling was performed by incubating 600 µL of
337 *bsuS*mc(C119S, C437S, C826S, E1118Q, R643C) (83 µM in 50 mM Tris-HCl pH 7.5, 200 mM NaCl) with
338 1 mM PEG2-biotin maleimide for 10 minutes at 4 °C. The reaction was quenched by addition of 0.5
339 mM 2-mercaptoethanol. Excess label was removed using Zeba spin desalting columns (Thermo
340 Fisher) in multiple parallel runs due to volume limitations. The final yield was 600 µL at 72.35 µM
341 (subunit concentration). Labelled *bsuS*mc(C119S, C437S, C826S, E1118Q, R643C) was loaded onto a
342 Superose 6 10/300 Increase column pre-equilibrated in 50 mM Tris-HCl pH 7.5, 200 mM NaCl. Peak
343 fractions were pooled and mixed with ScpA and ScpB at a 1:1:2 molar ratio relative to the *bsuS*mc
344 dimer. The final concentration of the full complex was adjusted to 5.7 µM. Complexes were aliquoted
345 in 100 µL portions, flash-frozen in liquid nitrogen, and stored at –80 °C.

346 **Purification of *bsu*ScpA**

347 ScpA was purified using the method described by (Vazquez Nunez, Ruiz Avila and Gruber, 2019). *E.*
348 *coli* BL21-Gold (DE3) cells, transformed with a pET-28 derived plasmid encoding the ScpA protein,
349 were used for expression. Cultivation was performed in ZYM-5052 autoinduction medium at 16°C for
350 28 hours. Cells were then harvested and resuspended in lysis buffer (50 mM Tris-HCl, pH 7.5; 200 mM
351 NaCl; 5% glycerol) supplemented with protease inhibitor cocktail. The cells were lysed by sonication,
352 and the lysate was clarified by centrifugation. The supernatant was applied to a 5 mL HiTrap Q ion

353 exchange column and eluted with a gradient up to 2 M NaCl. Peak fractions were pooled and adjusted
354 to a final concentration of 3 M NaCl by mixing with 4 M NaCl buffer. This mixture was loaded onto a
355 HiTrap Butyl HP column and eluted with a reverse gradient to 50 mM NaCl. Eluted peak fractions
356 were concentrated to 5 mL using Vivaspin 15 10K MWCO filters and further purified by size exclusion
357 chromatography (SEC) on a HiLoad 16/600 Superdex 75 pg column equilibrated with 20 mM Tris-HCl,
358 pH 7.5, and 200 mM NaCl. The purified protein was concentrated, flash frozen, and stored at -80°C.

359 **Purification of *bsu*ScpB**

360 ScpB was purified following the protocol outlined by (Vazquez Nunez, Ruiz Avila and Gruber, 2019).
361 The coding sequence of ScpB, cloned into a pET-22 derived plasmid, was transformed into chemically
362 competent BL21-Gold (DE3) *E. coli* cells. These cells were cultivated in ZYM-5052 autoinduction
363 medium at 24°C for 23 hours. Subsequently, the cells were harvested and resuspended in lysis buffer
364 (50 mM Tris-HCl, pH 7.5; 150 mM NaCl; 1 mM EDTA; 1 mM DTT) supplemented with protease
365 inhibitor cocktail. Cell lysis was performed by sonication, followed by centrifugation to remove cell
366 debris. The resulting supernatant was diluted to a final NaCl concentration of 50 mM and loaded onto
367 a 5 mL HiTrap Q HP column. Elution was achieved using a gradient up to 2 M NaCl. The eluate was
368 then diluted with lysis buffer containing 4 M NaCl to achieve a final concentration of 3 M NaCl. This
369 sample was applied to two 5 mL HiTrap Butyl columns connected in series, and the protein was
370 eluted with a reverse gradient to 50 mM NaCl. The peak fractions from this column were
371 concentrated and subjected to size exclusion chromatography (SEC) using a HiLoad 16/600 Superdex
372 200 pg column equilibrated with 50 mM Tris-HCl, pH 7.5, 100 mM NaCl, and 1 mM DTT. Fractions
373 containing ScpB were concentrated, flash frozen, and stored at -80°C.

374 **Medium scale sybody purification**

375 Individual sybody plasmids were transformed into chemically competent *E. coli* MC1061 cells via heat
376 shock at 42 °C for 45 s, followed by recovery in LB medium at 37 °C. Transformed cells were cultured
377 overnight in TB medium supplemented with 25 µg/ml chloramphenicol. Precultures were used to

378 inoculate 50 mL TB cultures, which were grown at 37 °C before shifting to 22 °C. Expression was
379 induced with 0.02% (wt/vol) L-(+)-arabinose and continued overnight at 22 °C with shaking. Cells
380 were harvested by centrifugation and resuspended in periplasmic extraction buffer. Following
381 incubation at 4 °C, cells were pelleted, and the supernatant was supplemented with imidazole to 15
382 mM. The extract was incubated with His MultiTrap HP resin, followed by centrifugation and washing
383 with TBS containing 30 mM imidazole. Elution was performed using TBS with 300 mM imidazole.
384 Purified sybodies were analyzed on a Sepax SRT-10C SEC100 column at 1 ml/min flow rate.
385 Monomeric sybodies eluted between 11–12.5 ml, while retention volumes <11 ml indicated
386 oligomerization, and >14 ml suggested strong column interaction. Non-expressed, oligomeric, or
387 highly interacting sybodies were discarded. Typical yields ranged from 200 µg to 1 mg (Zimmermann
388 *et al.*, 2020).

389 **Fluorescence imaging of ParB-GFP strains**

390 **Image acquisition**

391 *B. subtilis* cells were first cultured in LB supplemented with 5 µg/mL chloramphenicol and 0.5%
392 glucose at 30°C, from which a day culture was inoculated to 0.005 in LB with 5 µg/mL
393 chloramphenicol. When needed, cultures were induced at OD_{600} ~ 0.02 with 0.5% xylose and grown
394 an extra 30 minutes until imaging at an OD_{600} of 0.04. For microscopy analysis, 0.5 µL of the cell
395 suspension was spotted onto agarose-coated microscopy slides. Images were acquired using a Leica
396 DMi8 microscope equipped with an sCMOS DFC9000 (Leica) camera, a SOLA light engine (Lumencor),
397 and a 100×/1.40 oil-immersion objective. Exposure time for image acquisition was set to 600 ms.
398 Acquired images were processed using LAS X Office software (v.1.4.7.28982, Leica Microsystems).

399 **Image analysis**

400 Microscopy images were analyzed using a fully automated image processing pipeline. Cell
401 segmentation was performed with the pretrained Omnipose model (Cutler *et al.*, 2022) implemented
402 in Cellpose (Stringer *et al.*, 2021), which is optimized for bacterial morphologies. Prior to

403 segmentation, a normalization step was applied to standardize image contrast. Following
404 segmentation, intracellular foci were detected using Spotiflow (Mantes *et al.*, 2024), a dedicated
405 model trained for spot identification. Each detected spot was assigned to an individual cell based on
406 spatial location, enabling quantification of the number of foci per cell. Cell morphology analysis was
407 also performed to estimate cell length.

408 Quantitative results were compiled into a structured dataset, including the number of cells per image,
409 percentage of cells lacking foci, number of foci per cell, cell length, and number of foci per micron.
410 Data visualization and statistical analysis was performed using GraphPad Prism 10.4.1 (627).

411 **ATPase measurements**

412 ATPase activity was assessed using the coupled pyruvate kinase/lactate dehydrogenase reaction as
413 described by (Bürmann *et al.*, 2017). ADP production was monitored over a period of 1 hour by
414 measuring the absorbance changes of NADH at 340 nm. Data collection was performed using a
415 Synergy Neo Hybrid Multi-Mode Microplate Reader. The reaction mixture comprised 1 mM NADH, 3
416 mM phosphoenolpyruvic acid, 100 U pyruvate kinase, 20 U lactate dehydrogenase, and varying
417 concentrations of ATP. For assays requiring double-stranded oligonucleotides, a 40 bp oligonucleotide
418 (5'-TTAGTTGTTC GTAGTGCTCG TCTGGCTCTG GATTACCCGC-3') was added to a final concentration of 3
419 mM. The final protein concentration in the assay was 0.15 µM *bsuS*mc dimers in ATPase assay buffer
420 (50 mM HEPES-KOH, pH 7.5; 50 mM NaCl; 2 mM MgCl2). All measurements were conducted at 25°C.

421 **Acknowledgments**

422 We are grateful to Roberto Vazquez Nunez for the biotinylated *bsuS*mc(C119S, C437S, C826S,
423 E1118Q, R643C) protein preparation, Arianna Ravera from the DCSR computing facility for help in
424 image analysis and data extraction of the fluorescence microscopy images. Members of the Gruber
425 Lab for critical feedback of the manuscript and for stimulating discussions.

426 **Funding**

This study was supported by internal funding and by the European Research Council (Horizon 2020 ERC CoG 724482).

Author contributions

O.G. performed all *in vivo* experiments from sybody selection, fluorescence microscopy imaging, chimeric phenotypic screen. M.T. and L.H-H. performed the *in vitro* sybody screening (ribosome display, phage display, and first sybody purification). O.G. performed protein purifications, cross-linking and ATPase measurements, as well as data analysis, figures and writing. O.G. wrote the first manuscript draft. All authors reviewed and edited the manuscript. Funding acquisition and supervision, S.G.

Competing interests

The authors declare that they have no competing interests.

Data and materials availability

All raw data will be made available at Mendeley Data DOI: 10.17632/k6k62p7z2s.1 (https://data.mendeley.com/datasets/k6k62p7z2s/1).

443 **Figure Legends**

444 **Figure 1: Selection of sybodies targeting *S*mc-ScpAB in *B. subtilis*.**

445 **(A) (i)** Structural design and randomization scheme of the three synthetic sybody libraries: concave,
446 loop, and convex. Complementarity-determining regions (CDRs) 1, 2, and 3 are shown in yellow,
447 orange, and red, respectively; randomized residues are shown as sticks. Adapted from (I.
448 Zimmermann *et al.*, 2018). **(ii)** SMC domain organization. The N- and C-terminal regions encode half
449 an ATPase head, while the middle domain constitutes the hinge dimerization domain. The elongated
450 sequence in-between encodes for long helical sequences that will form an antiparallel intramolecular
451 coiled coil. Hd: head, Hng: hinge, 4N: 4N arm-to-arm contact, J: joint. **(iii)** SMC complexes harbor
452 juxtaposed arms in their resting state. Upon ATP binding at the heads, the heads dimerize (head
453 engagement), leading to a conformational change of the entire complex in which the arms open. This
454 state is thought to fit a loop of DNA (not shown) in the S compartment formed by the SMC arms, that
455 will be pushed towards the K compartment formed by the heads and kleisin, after ADP release. We
456 hypothesized that SMC-blocking sybodies can stabilize distinct conformation of the *bsuS*mc-ScpAB
457 complex promoted by ATP hydrolysis and DNA binding, potentially inducing a *Δsmc*-like phenotype *in*
458 *vivo* and enabling biochemical characterization of trapped conformations *in vitro*. Blue: SMC dimer,
459 Green: kleisin ScpA. The ScpB KITE subunits are not represented for the sake of simplicity. HngDBS:
460 Hinge DNA-binding site, HdDBS: Head DNA-binding site.

461 **(B)** Framework for sybody selection. *In vitro* selection starts with ~10^{12} sybody variants per library
462 subjected to ribosome display for pre-enrichment, followed by two rounds of phage display. For *in*
463 *vivo* selection, 95 randomly selected sybody genes were integrated into the *B. subtilis* chromosome
464 under the control of a xylose-inducible promoter by allelic replacement at the *amyE* locus. Growth
465 defects on rich medium were tested on ONA agar plates with or without 0.5% xylose. Example
466 shown: Sb164 (loop library) did not affect growth, whereas Nb31 impaired growth upon induction,
467 suggesting interference with *bsuS*mc function.

468 **(C)** Growth assay results for the 95 *B. subtilis* strains expressing individual xylose-inducible sybodies of
469 the loop library. Bars show colony counts "without" (green) on top of "with" (pink) xylose. Strains are
470 ordered by their original position in the 96-well plate. Fourteen sybodies consistently impaired colony
471 formation under inducing conditions (marked by dotted lines). Sybody numbers indicated above the
472 plots correspond to selected candidates used in subsequent experiments, numbering according to
473 order of first use. Notably, the strain corresponding to the E09 sybody (Sb018), showed an absence of
474 colonies upon sybody induction. However, this sybody candidate gave intermediate phenotypes in
475 later experiments, which is why it was excluded from detailed analysis.

476

477 **Figure 2: Sybody-induced chromosome segregation defects visualized by ParB-GFP imaging.**
478 **(A)** i, *Top*: Schematic illustrating ParB-GFP binding near *oriC*, enabling visualization of origin
479 positioning. *Bottom*: Representative images showing ParB-GFP foci in wild-type and *Δsmc B. subtilis*.
480 *Smc* WT cells typically display 2–4 foci per cell, whereas *Δsmc* cells exhibit reduced foci numbers. ii,
481 Number of ParB-GFP foci per µm of cell length in a strain carrying inducible sybody Sb006. A
482 significant decrease in foci is detected from 40 minutes post-induction (p_{0-10} = 0.9674; p_{0-20} =
483 0.9033; p_{0-30} = 0.3744; p_{0-40} = 0.0145; p_{0-50} = 0.0004; p_{0-60} < 0.001). Based on this, a
484 standardized induction time of ~35 minutes was used in all subsequent experiments.

485 **(B)** ParB-GFP foci density (foci/µm) in WT, Δsmc, and sybody-expressing strains after 35 minutes of
486 xylose induction. Violin plots show distribution per condition; solid lines denote the mean, and
487 dotted lines indicate quartiles.

488 **(C)** Spot assay to assess colony formation of *B. subtilis* strains *bsu* or *spn* variants of *S*mc-ScpAB and
489 ParB. *Top*: Schematic shows gene origins (blue: *B. subtilis*; grey: *S. pneumoniae*). The leftmost column
490 corresponds to the parental *B. subtilis* strain 1A700 carrying the *S. pneumoniae* genes without
491 chloramphenicol resistance (non-growing). The next spots represent the same strains carrying no
492 sybody gene but the Cm resistance (EV for empty vector). Remaining spots are sybody-expressing

493 strains; sybody numbers are indicated above. Cells were grown for 16 h at 37 °C on ONA
494 supplemented with 0.5% xylose and chloramphenicol. Hd: head, Hng: hinge, 4N: 4N arm-to-arm
495 contact, J: joint.

496

497 **Figure 3: Mapping sybody binding sites on Smc-ScpAB.**

498 **(A)** Colony formation of *B. subtilis* strains expressing chimeric Smc-ScpAB complexes comprising *S.*
499 *pneumoniae* and *B. subtilis* sequences. The schematic above the spot assay depicts the species origin
500 of the *smc* gene, the *scpAB* operon and *parB* gene (blue: *B. subtilis*; grey: *S. pneumoniae*). "–"
501 indicates no insertion at the *amyE* locus; "EV" refers to the empty vector control containing only the
502 chloramphenicol resistance cassette that was inserted in *amyE*; numbered labels correspond to
503 sybodies. Cells were spotted on rich medium (ONA) supplemented with chloramphenicol and xylose
504 and incubated for 16 h at 37 °C. Hd: head, Hng: hinge, 4N: 4N arm-to-arm contact, J: joint.

505 **(B)** ATP hydrolysis rates of *bsu*Smc-ScpAB in the presence of sybodies but absence of DNA. Significant
506 effects by one-way ANOVA are indicated by p values.

507 **(C)** ATPase rates in the presence of 40 bp dsDNA. All sybodies significantly reduced DNA-stimulated
508 ATP hydrolysis. Reported p-values: Sb020 ($p = 0.340$), Sb194 ($p = 0.0049$), Sb002 ($p = 0.0007$), Sb015
509 ($p = 0.0003$); all others, $p < 0.0001$.

510 **(D)** Schematic summary of sybody binding sites mapped onto the Smc dimer, categorized by their
511 effect on ATPase activity. Sybodies are grouped based on functional impact and mapped to
512 corresponding structural regions: pink/yellow boxes indicate residues 318–339 and 836–857; green
513 boxes mark residues 248–276 and 899–927; and the red box highlights the 4N contact region (approx.
514 residues 290–320).

515

516 **Figure 4: Proposed models for sybody interactions with *bsuS*mc-ScpAB during the ATPase cycle.**

517 Model for sybodies of the Opening^{UP}, Closing^{UP} and Closing^{DOWN} group. Opening^{UP} sybodies, likely
518 prevent complete arm closure. In the presence of DNA, these sybodies may stabilize a suboptimal
519 conformation for head disengagement, resulting in reduced ATPase activity (not shown here).
520 Closing^{UP} and Closing^{DOWN} sybodies stabilize a closed-arm conformation. These likely hinder DNA
521 segments from entering the inter-arm space and accessing the hinge-proximal DNA binding site.

522

523 **Figure S1: Preparation of *bsuS*mc(C119S, C437S, C826S, E1118Q, R643C)-ScpAB complex and loop**
524 **extrusion model**

525 **(A)** Size-exclusion chromatography profile of biotinylated *bsuS*mcE(C119S, C437S, C826S, E1118Q,
526 R643C)-ScpAB complex. Peak fractions (elution at ~13 mL, pooled fractions indicated by dotted lines
527 for a final volume of 1.8 mL) were collected for downstream use; the final concentration was 5.9 µM
528 (dimer). * : A secondary peak appeared at ~14 mL; its identity was uncertain and was excluded from
529 the peak. SDS-PAGE confirms successful biotinylation of the *bsu*Smc(C119S, C437S, C826S, E1118Q,
530 R643C)-ScpAB complex.

531 **(B)** Segment-capture model for *bsuS*mc-ScpAB, in which ATP binding and hydrolysis drive transitions
532 between open and closed conformations to mediate loop extrusion.

533

534 **Figure S2: Representative results from *in vivo* sybody selection based on colony formation.**

535 **(A)** Representative examples of *in vivo* transformation assays for nine sybody-expressing *B. subtilis*
536 strains. Sybody genes were integrated into the *amyE* locus under xylose-inducible control.
537 Transformants were grown on oxoid nutrient agar (ONA) plates supplemented with chloramphenicol
538 and 0.5% xylose to assess growth defects. Shown are candidates from the concave library: Sb051
539 (well B08) and Sb078 (D12). Loop library: Sb007 (E05), Sb020 (E12), Sb031 (F05), Sb164 (D12) and
540 NbH07 (Sb194). Convex library: Sb239 (D12) and Sb248 (E10).

541 **(B)** Growth assay results for the 285 *B. subtilis* strains expressing individual xylose-inducible sybodies.
542 Bars show each colony counts "without" (green) on top of "with" (pink) xylose. Strains are ordered by
543 their original 96-well plate. Only the loop library yielded sybodies that consistently impaired growth
544 under inducing conditions (dotted line). Sybody numbers indicated above the plots correspond to
545 positive candidates used in subsequent experiments, numbered according to order of use. Notably,
546 the strain corresponding to the E09 M sybody (Sb018), also showed an absence of growth upon

547 sybody induction. However, this sybody candidate gave intermediate phenotypes in later
548 experiments, which is why it was excluded from this study. Results for the loop library are also shown
549 in Figure 1.

550

551 **Figure S3: Functional impact of sybody expression on chromosome organization, cell length, and**
552 **growth in *B. subtilis*.**

553 **(A)** Average number of ParB-GFP foci per µm of cell length in strains expressing individual sybodies,
554 with and without xylose induction. Most uninduced strains differed significantly from the Smc WT
555 control, likely due to leaky expression from the P_{xyl} ($p < 0.0001$), except Sb015 ($p > 0.9999$), Sb156
556 ($p = 0.2345$), and Sb016 (negative control, $p > 0.9999$).

557 **(B)** Average cell length across the same conditions, measured in ParB-GFP strains with or without
558 Smc, and with or without each sybody. Bars indicate standard deviation. Tested sybodies caused cell
559 elongation, a characteristic phenotype of impaired Smc activity, as chromosome segregation defects
560 delay cell division, with mean lengths from 4.70 ± 2.16 µm (Sb020) to 8.68 ± 2.99 µm (Sb010),
561 compared to 4.51 ± 1.95 µm in wild-type and 9.96 ± 8.92 µm in Δ*smc*. **(C)** Growth curves of *B. subtilis*
562 strains expressing individual sybodies compared to the WT strain, with and without xylose induction.
563 Each curve represents the mean of two biological replicates. Six sybodies were randomly picked and
564 showed in this figure. Fluorophore-free strains showed wild type-like growth without xylose but
565 strong delays post-induction, followed by partial growth recovery after 12 hours, likely due to xylose
566 depletion or suppressor emergence. In sybody-expressing strains, a clear drop in cell density was
567 observed ~2.5 hours post-induction.

568

569 **Figure S4: ATPase hydrolysis rate of the *bsuS*mc-ScpAB complex with each selected sybody and**
570 **viability of *B. subtilis* strains expressing chimeric Smc-ScpAB complexes in the absence of sybody**
571 **induction.**

572 **(A)** Spotting assay assessing the growth of *B. subtilis* strains carrying chimeric Smc-ScpAB operons
573 composed of *S. pneumoniae* and *B. subtilis* components. Strains harbor individual sybody constructs
574 integrated at the *amyE* locus under control of a xylose-inducible promoter but were grown without
575 inducer. "–" indicates no integration at *amyE*; "EV" corresponds to an empty vector control containing
576 only the chloramphenicol resistance cassette. Numbered labels indicate strains carrying specific
577 sybody constructs. Cells were spotted on rich medium (ONA) containing chloramphenicol and
578 incubated for 16 h at 37 °C.

579 **(B)** Overall ATPase hydrolysis rate of the *bsuS*mc-ScpAB complex in presence of each sybody and +/-
580 DNA. Sb06, 021 and 194 triggered a significant difference in ATP hydrolysis between +/- dsDNA
581 conditions. The rest is non-significant.

582

583 **Figure S5: Hypothetical model for an Opening^{DOWN} class of sybodies, not recovered in this study.**

584 This may indicate that stabilizing an open conformation near the ATPase heads does not interfere
585 with Smc function.

586

587 **Tables**

588 **Table 1: Sybody enrichments at different steps of the selection procedure.**

589 Ribosome display output was quantified by qPCR, while phage display results include final phage

590 titers and enrichment values from rounds one and two, also measured by qPCR.

591 **Table S1: Sybody sequences**

592 **Table S2: Percentage of cells lacking ParB-GFP foci**, indicating the absence of chromosome due to

593 segregation defect. In presence and absence of xylose for sybody induction.

594 **Table S3: Strains**

595 **Table S4: Plasmids**

596 **Table S5: Oligonucleotides**

597

598 **References**

599 Bock, F.P. *et al.* (2022) "A joint-ParB interface promotes Smc DNA recruitment," *Cell reports*, 40(9), p.
600 111273. Available at: https://doi.org/10.1016/J.CELREP.2022.111273.

601 Bürmann, F. *et al.* (2013) "An asymmetric SMC-kleisin bridge in prokaryotic condensin," *Nature*
602 *Structural & Molecular Biology*, 20(3), pp. 371–379. Available at: https://doi.org/10.1038/nsmb.2488.

603 Bürmann, F. *et al.* (2017) "Tuned SMC Arms Drive Chromosomal Loading of Prokaryotic Condensin,"
604 *Molecular Cell*, 65(5), pp. 861-872.e9. Available at: https://doi.org/10.1016/j.molcel.2017.01.026.

605 Bürmann, F. and Gruber, S. (2015) "SMC condensin: promoting cohesion of replicon arms," *Nature*
606 *Structural & Molecular Biology 2015 22:9*, 22(9), pp. 653–655. Available at:
607 https://doi.org/10.1038/nsmb.3082.

608 Cutler, K.J. *et al.* (2022) "Omnipose: a high-precision morphology-independent solution for bacterial
609 cell segmentation," *Nature Methods*, 19(11), pp. 1438–1448. Available at:
610 https://doi.org/10.1038/s41592-022-01639-4.

611 Deneka, D. *et al.* (2021) "Allosteric modulation of LRRC8 channels by targeting their cytoplasmic
612 domains," *Nature Communications*, 12(1), p. 5435. Available at: https://doi.org/10.1038/s41467-021-
613 25742-w.

614 Dénéréaz, J. and Veening, J.-W. (2024) "BactEXTRACT: an R Shiny app to quickly extract, plot and
615 analyse bacterial growth and gene expression data," *Access Microbiology*, 6(1), p. 000742.v3.
616 Available at: https://doi.org/10.1099/acmi.0.000742.v3.

617 Diebold-Durand, M.L. *et al.* (2017) "Structure of Full-Length SMC and Rearrangements Required for
618 Chromosome Organization," *Molecular Cell*, 67(2), pp. 334-347.e5. Available at:
619 https://doi.org/10.1016/j.molcel.2017.06.010.

620 Diebold-Durand, M.-L., Bürmann, F. and Gruber, S. (2019) "High-Throughput Allelic Replacement
621 Screening in <Emphasis Type="Italic">Bacillus subtilis</Emphasis>," *Methods in Molecular Biology*,
622 2004, pp. 49–61. Available at: https://doi.org/10.1007/978-1-4939-9520-2_5.

623 Gabler, F. *et al.* (2020) "Protein Sequence Analysis Using the MPI Bioinformatics Toolkit," *Current*
624 *Protocols in Bioinformatics*, 72(1), p. e108. Available at: https://doi.org/10.1002/cpbi.108.

625 Gruber, S. *et al.* (2014) "Interlinked Sister Chromosomes Arise in the Absence of Condensin during
626 Fast Replication in B. subtilis," *Current Biology*, 24(3), pp. 293–298. Available at:
627 https://doi.org/10.1016/J.CUB.2013.12.049.

628 Hirano, M. and Hirano, T. (2004) "Positive and negative regulation of SMC-DNA interactions by ATP
629 and accessory proteins," *The EMBO journal*, 23(13), pp. 2664–2673. Available at:
630 https://doi.org/10.1038/sj.emboj.7600264.

631 Hutter, C.A.J. *et al.* (2019) "The extracellular gate shapes the energy profile of an ABC exporter,"
632 *Nature Communications*, 10(1). Available at: https://doi.org/10.1038/s41467-019-09892-6.

633 Jumper, J. *et al.* (2021) "Highly accurate protein structure prediction with AlphaFold," *Nature*,
634 596(7873), pp. 583–589. Available at: https://doi.org/10.1038/s41586-021-03819-2.

Kruse, A.C. *et al.* (2013) “Activation and allosteric modulation of a muscarinic acetylcholine receptor,” *Nature*, 504(7478), pp. 101–106. Available at: https://doi.org/10.1038/nature12735.

Liu, H.W. *et al.* (2025) “The SMC Hinge is a Selective Gate for Obstacle Bypass.” bioRxiv, p. 2025.03.17.643644. Available at: https://doi.org/10.1101/2025.03.17.643644.

Mantes, A.D. *et al.* (2024) “Spotiflow: accurate and efficient spot detection for fluorescence microscopy with deep stereographic flow regression.” bioRxiv, p. 2024.02.01.578426. Available at: https://doi.org/10.1101/2024.02.01.578426.

Marko, J.F. *et al.* (2019) “DNA-segment-capture model for loop extrusion by structural maintenance of chromosome (SMC) protein complexes,” *Nucleic Acids Research*, 47(13), pp. 6956–6972. Available at: https://doi.org/10.1093/nar/gkz497.

Minnen, A. *et al.* (2016) “Control of Smc Coiled Coil Architecture by the ATPase Heads Facilitates Targeting to Chromosomal ParB/parS and Release onto Flanking DNA,” *Cell Reports*, 14. Available at: https://doi.org/10.1016/j.celrep.2016.01.066.

Pacesa, M. *et al.* (2025) “One-shot design of functional protein binders with BindCraft,” *Nature*, pp. 1–10. Available at: https://doi.org/10.1038/s41586-025-09429-6.

Rasmussen, Søren G.F. *et al.* (2011) “Structure of a nanobody-stabilized active state of the β(2) adrenoceptor,” *Nature*, 469(7329), pp. 175–181. Available at: https://doi.org/10.1038/NATURE09648.

Rasmussen, Søren G. F. *et al.* (2011) “Structure of a nanobody-stabilized active state of the β2 adrenoceptor,” *Nature*, 469(7329), pp. 175–180. Available at: https://doi.org/10.1038/nature09648.

Seeger, M.A. *et al.* (2012) “Tuning the Drug Efflux Activity of an ABC Transporter in vivo by in vitro Selected DARPin Binders,” *PLoS ONE*, 7(6), p. e37845. Available at: https://doi.org/10.1371/journal.pone.0037845.

Soh, Y.M. *et al.* (2015) “Molecular basis for SMC rod formation and its dissolution upon DNA binding,” *Molecular cell*, 57(2), pp. 290–303. Available at: https://doi.org/10.1016/J.MOLCEL.2014.11.023.

Stringer, C. *et al.* (2021) “Cellpose: a generalist algorithm for cellular segmentation,” *Nature Methods*, 18(1), pp. 100–106. Available at: https://doi.org/10.1038/s41592-020-01018-x.

Sullivan, N.L., Marquis, K.A. and Rudner, D.Z. (2009) “Recruitment of SMC by ParB-parS Organizes the Origin Region and Promotes Efficient Chromosome Segregation,” *Cell*, 137(4), pp. 697–707. Available at: https://doi.org/10.1016/J.CELL.2009.04.044.

Vazquez Nunez, R. *et al.* (2021) “Gradual opening of Smc arms in prokaryotic condensin,” *Cell Reports*, 35(4), p. 109051. Available at: https://doi.org/10.1016/J.CELREP.2021.109051.

Vazquez Nunez, R., Ruiz Avila, L.B. and Gruber, S. (2019) “Transient DNA Occupancy of the SMC Interarm Space in Prokaryotic Condensin,” *Molecular Cell*, 75(2), pp. 209-223.e6. Available at: https://doi.org/10.1016/j.molcel.2019.05.001.

Wang, X. *et al.* (2014) “The SMC condensin complex is required for origin segregation in Bacillus subtilis,” *Current Biology*, 24(3), pp. 287–292. Available at: https://doi.org/10.1016/j.cub.2013.11.050.

Wang, X. *et al.* (2017) "Bacillus subtilis SMC complexes juxtapose chromosome arms as they travel from origin to terminus," *Science*, 355(6324), pp. 524–527. Available at: https://doi.org/10.1126/science.aai8982.

Yatskevich, S., Rhodes, J. and Nasmyth, K. (2019) "Organization of Chromosomal DNA by SMC Complexes," *Annual review of genetics*, 53, pp. 445–482. Available at: https://doi.org/10.1146/ANNUREV-GENET-112618-043633.

Zimmermann, I. *et al.* (2018) "Synthetic single domain antibodies for the conformational trapping of membrane proteins," *eLife*, 7. Available at: https://doi.org/10.7554/eLife.34317.

Zimmermann, I. *et al.* (2020) "Generation of synthetic nanobodies against delicate proteins," *Nature Protocols*, 15(5), pp. 1707–1741. Available at: https://doi.org/10.1038/s41596-020-0304-x.

Zimmermann, L. *et al.* (2018) "A Completely Reimplemented MPI Bioinformatics Toolkit with a New HHpred Server at its Core," *Journal of Molecular Biology*, 430(15), pp. 2237–2243. Available at: https://doi.org/10.1016/j.jmb.2017.12.007.

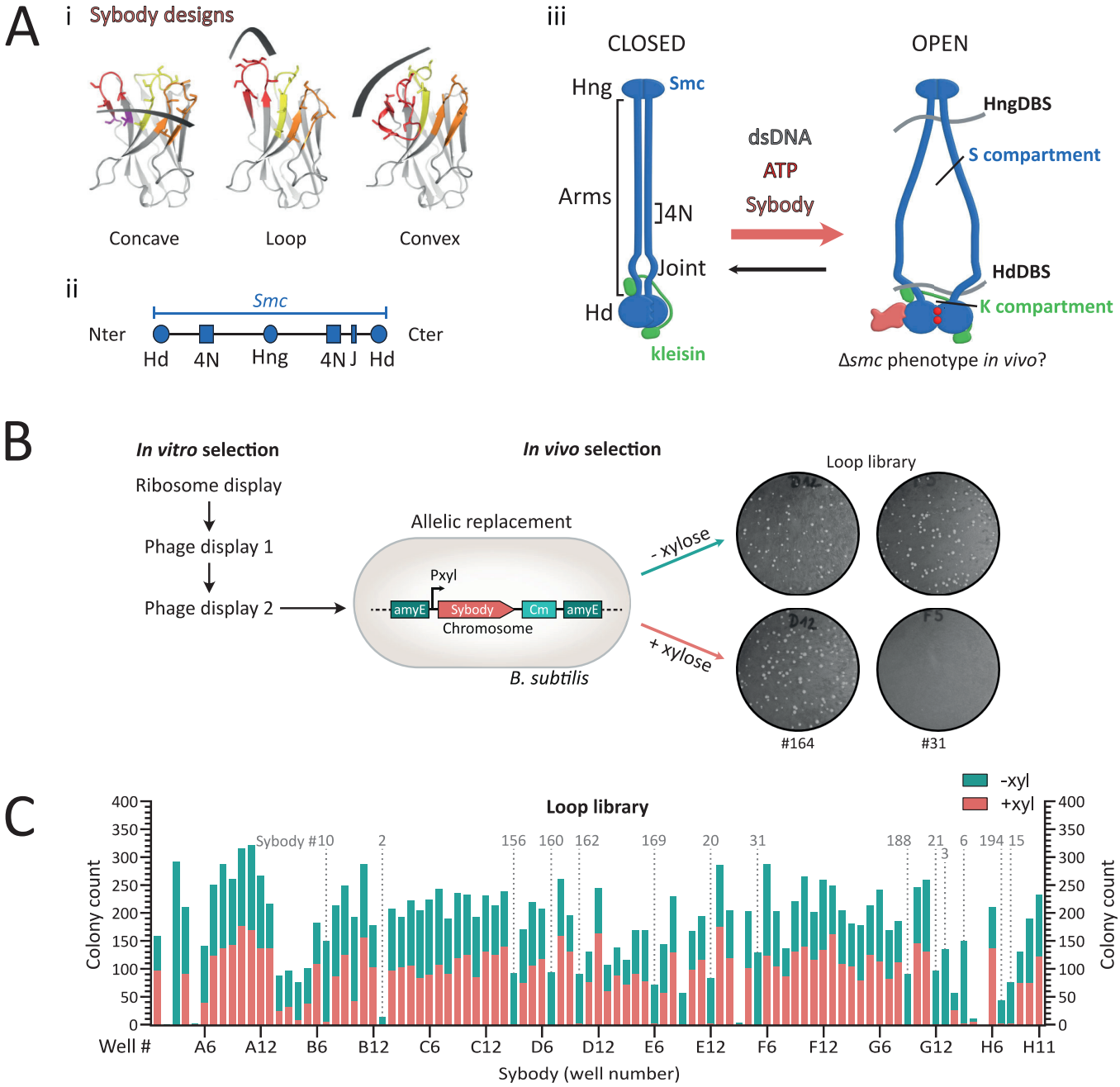
A
i Sybody designs
Concave
Loop
Convex
ii
Smc
Nter
Cter
Hd
4N
Hng
4N J
Hd
iii
CLOSED
OPEN
Hng
Smc
Arms
]4N
Joint
Hd
kleisin
dsDNA
ATP
Sybody
HngDBS
S compartment
HdDBS
K compartment
Δsmc phenotype in vivo?
B
In vitro selection
Ribosome display
Phage display 1
Phage display 2
In vivo selection
Allelic replacement
Pxyl
amyE
Sybody
Cm
amyE
Chromosome
B. subtilis
- xylose
+ xylose
Loop library
#164
#31
C
Loop library
-xyl
+xyl
Colony count
Sybody #10
2
156
160
162
169
20
31
188
21
3
6
194
15
Well #
A6
A12
B6
B12
C6
C12
D6
D12
E6
E12
F6
F12
G6
G12
H6
H11
Sybody (well number)

Figure 1

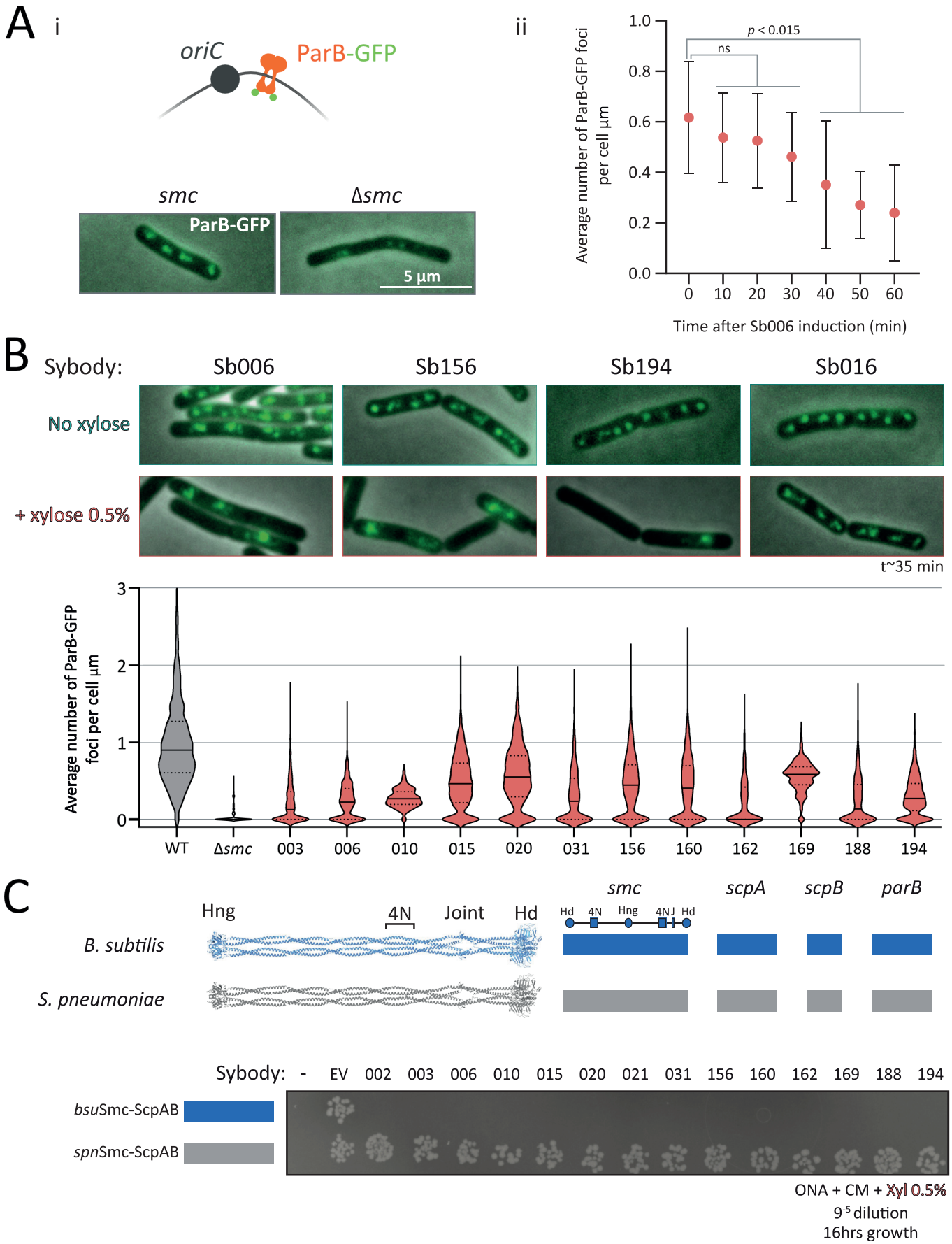
A
i
oriC
ParB-GFP
smc
Δsmc
ParB-GFP
5 µm
ii
Average number of ParB-GFP foci per cell µm
p < 0.015
ns
Time after Sb006 induction (min)
B
Sybody:
Sb006
Sb156
Sb194
Sb016
No xylose
+ xylose 0.5%
t~35 min
Average number of ParB-GFP foci per cell µm
WT
Δsmc
003
006
010
015
020
031
156
160
162
169
188
194
C
Hng
4N
Joint
Hd
smc
scpA
scpB
parB
B. subtilis
S. pneumoniae
Sybody:
EV
002
003
006
010
015
020
021
031
156
160
162
169
188
194
bsuSmc-ScpAB
spnSmc-ScpAB
ONA + CM + Xyl 0.5%
9-5 dilution
16hrs growth

Figure 2

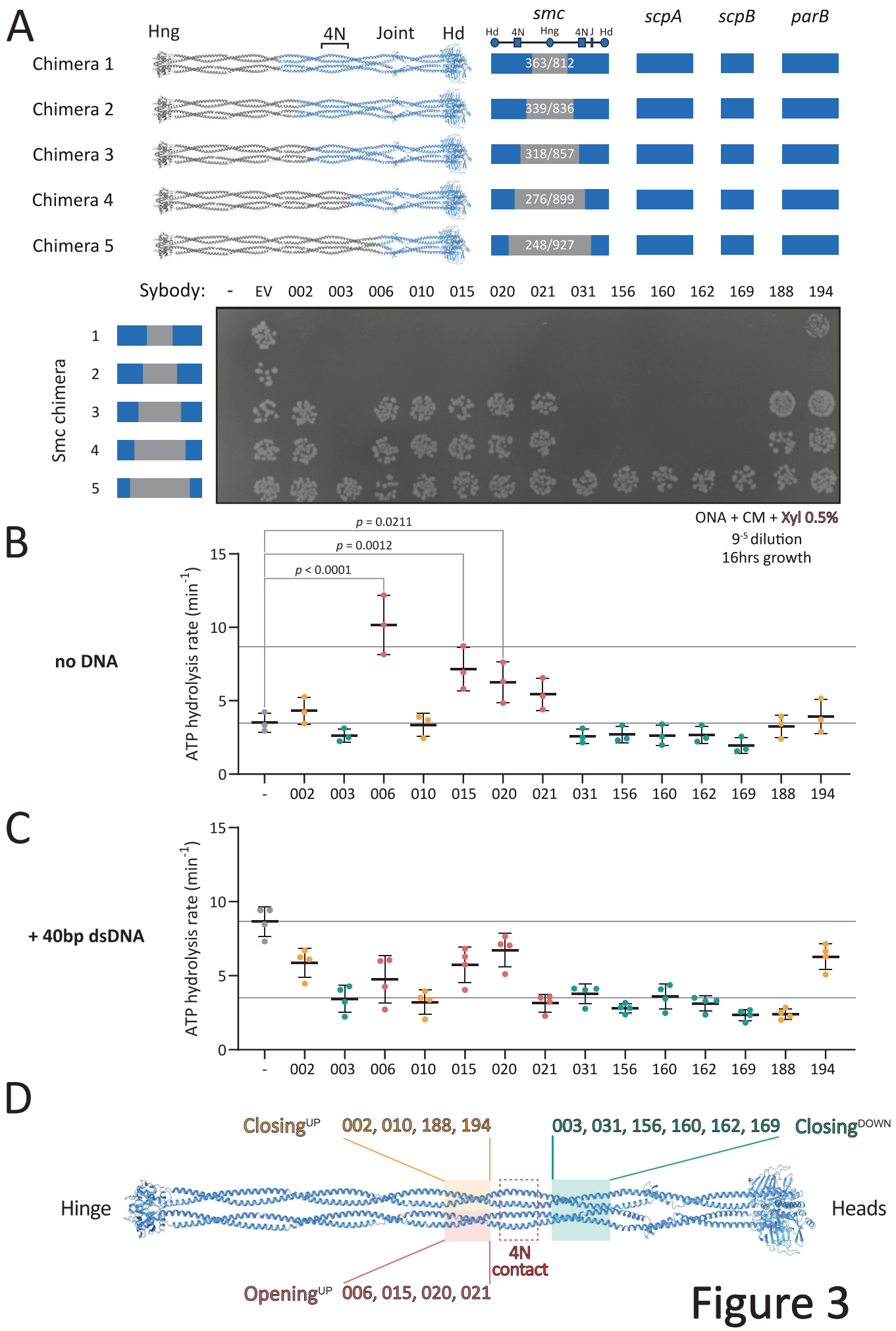
A
Hng
4N
Joint
Hd
smc
Hd 4N Hng 4NJ Hd
scpA
scpB
parB
Chimera 1
Chimera 2
Chimera 3
Chimera 4
Chimera 5
363/812
339/836
318/857
276/899
248/927
Sybody: - EV 002 003 006 010 015 020 021 031 156 160 162 169 188 194
Smc chimera
1
2
3
4
5
ONA + CM + Xyl 0.5%
9-5 dilution
16hrs growth
B
no DNA
p = 0.0211
p = 0.0012
p < 0.0001
ATP hydrolysis rate (min-1)
0
5
10
15
- 002 003 006 010 015 020 021 031 156 160 162 169 188 194
C
+ 40bp dsDNA
ATP hydrolysis rate (min-1)
0
5
10
15
- 002 003 006 010 015 020 021 031 156 160 162 169 188 194
D
ClosingUP 002, 010, 188, 194
003, 031, 156, 160, 162, 169 ClosingDOWN
Hinge
Heads
4N contact
OpeningUP 006, 015, 020, 021

Figure 3

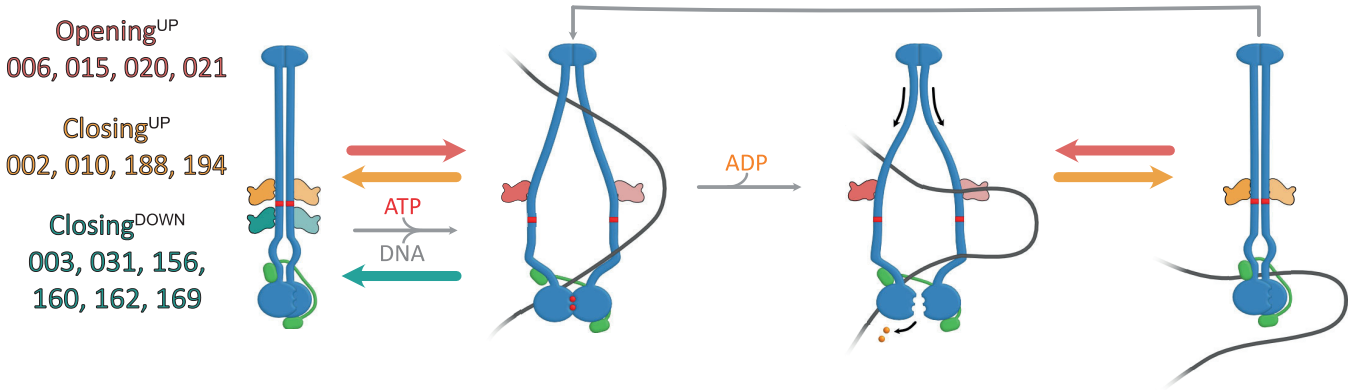
Opening^UP
006, 015, 020, 021
Closing^UP
002, 010, 188, 194
Closing^DOWN
003, 031, 156,
160, 162, 169
ATP
DNA
ADP

Figure 4

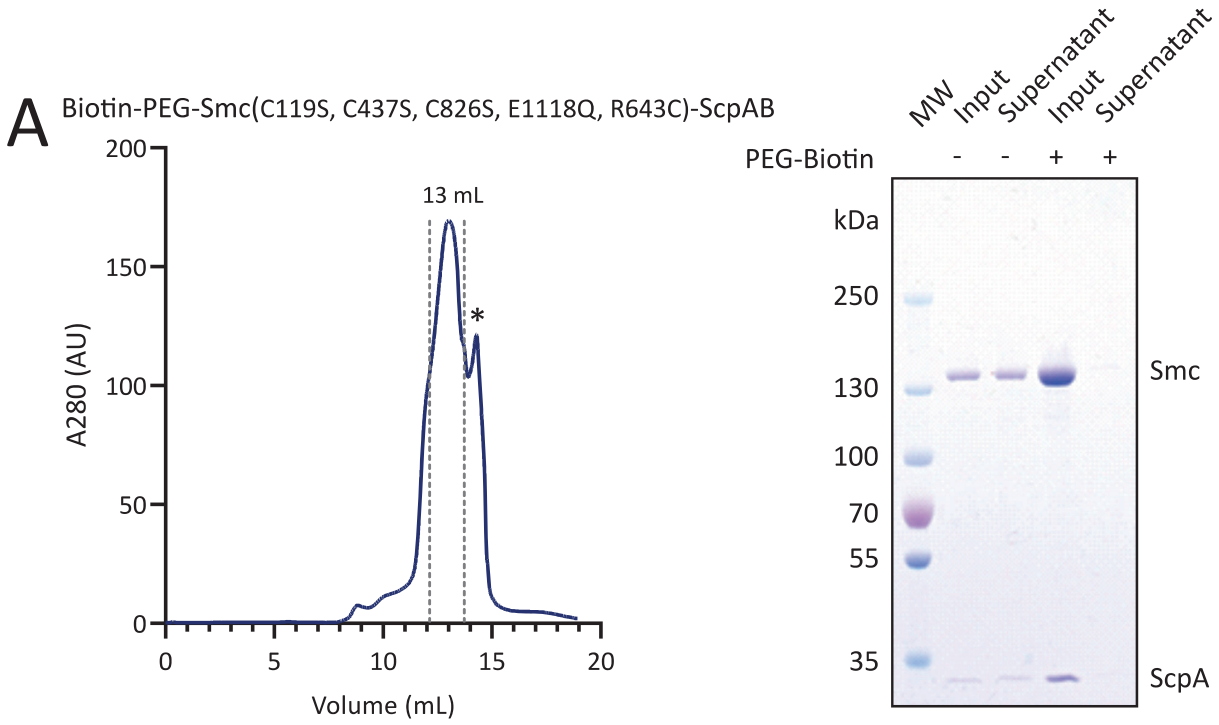
A
Biotin-PEG-Smc(C119S, C437S, C826S, E1118Q, R643C)-ScpAB
13 mL
*
A280 (AU)
Volume (mL)
MW
Input
Supernatant
Input
Supernatant
PEG-Biotin
- - + +
kDa
250
130
100
70
55
35
Smc
ScpA

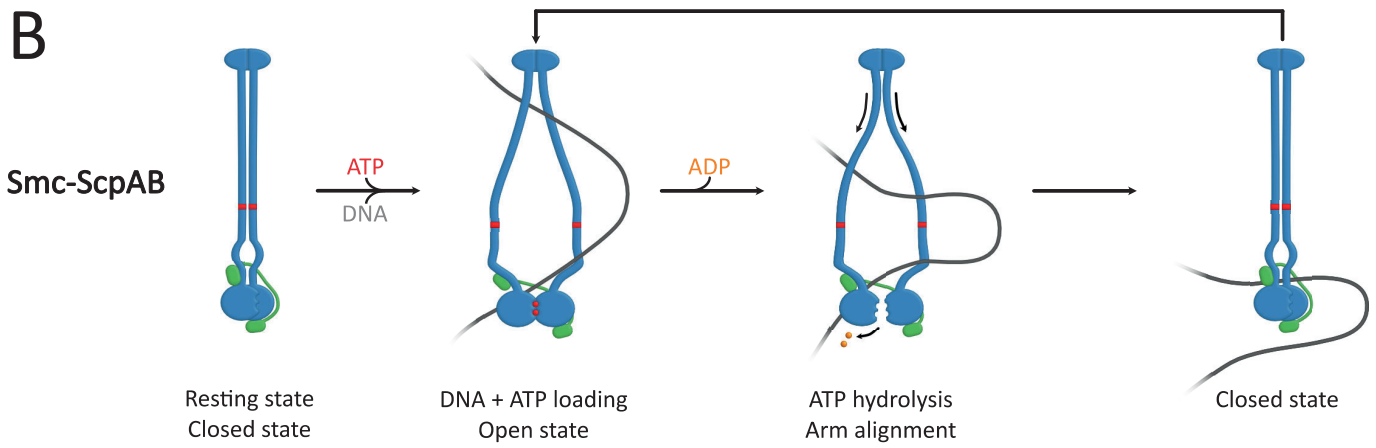
B
Smc-ScpAB
ATP
DNA
ADP
Resting state
Closed state
DNA + ATP loading
Open state
ATP hydrolysis
Arm alignment
Closed state

Figure S1

Figure S2

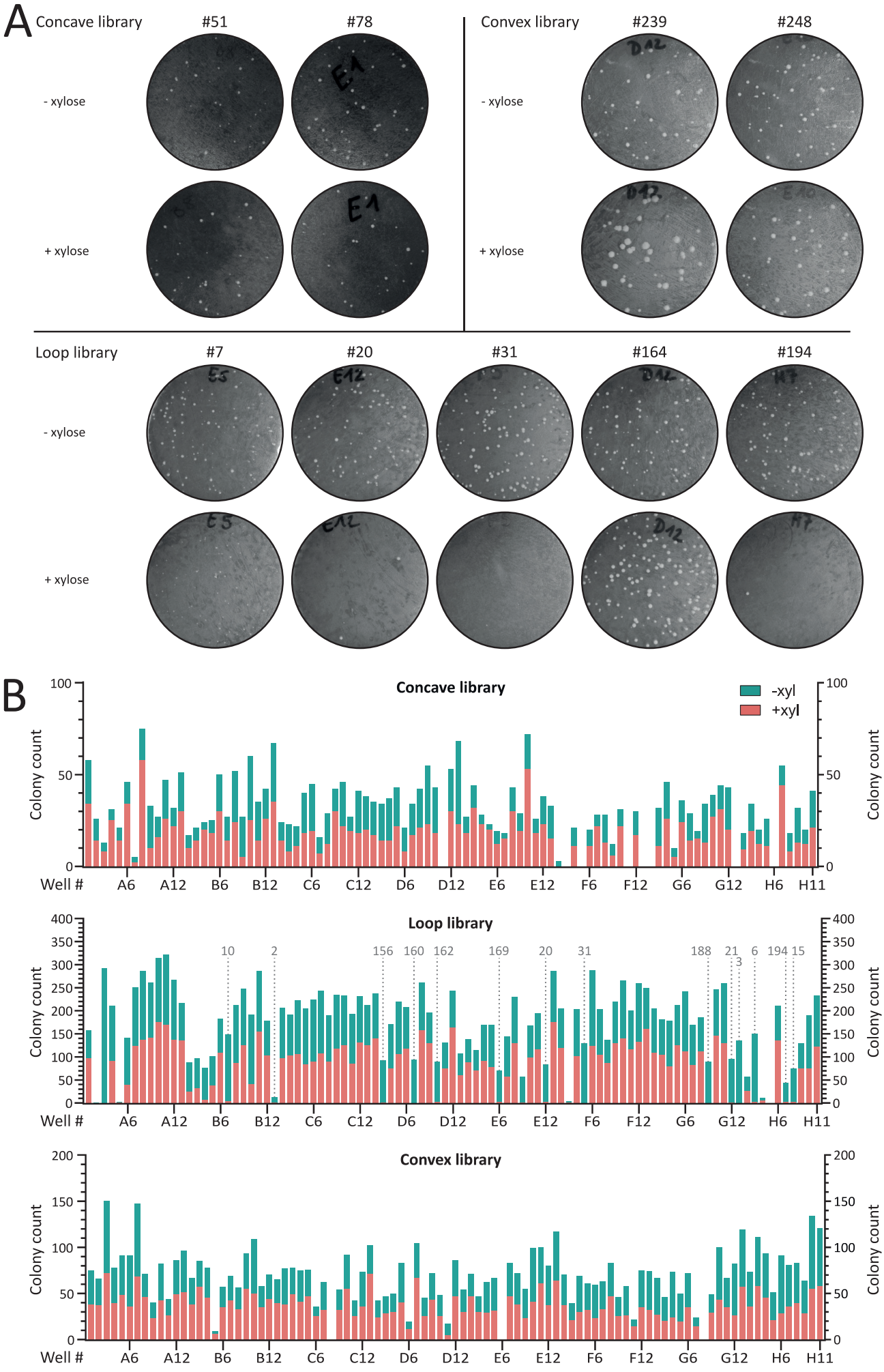
A
Concave library
#51
#78
Convex library
#239
#248
- xylose
+ xylose
Loop library
#7
#20
#31
#164
#194
B
Concave library
-xyl
+xyl
Colony count
Well #
A6
A12
B6
B12
C6
C12
D6
D12
E6
E12
F6
F12
G6
G12
H6
H11
Loop library
10
2
156
160
162
169
20
31
188
21
3
6
194
15
Convex library

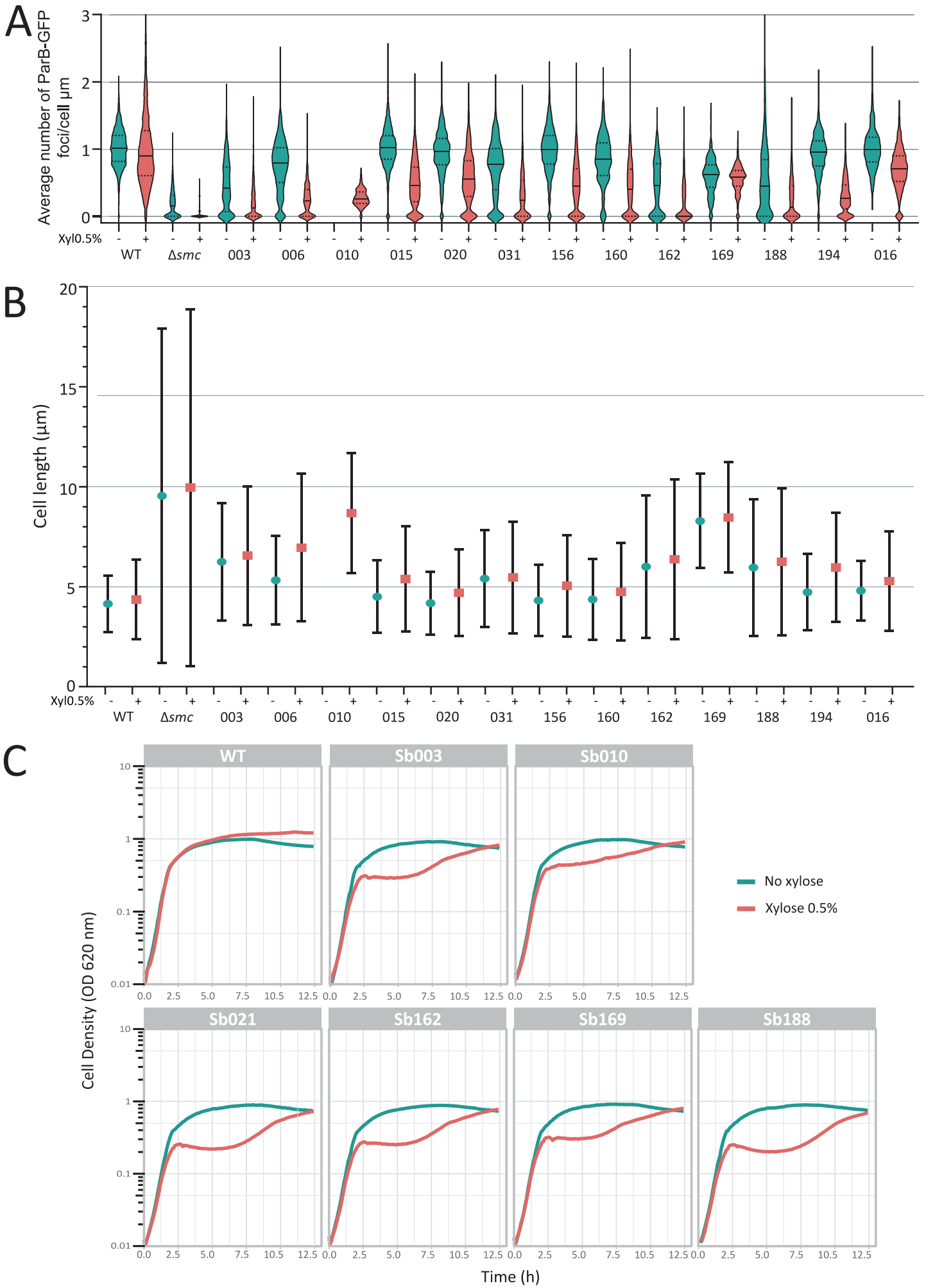
A
Average number of ParB-GFP foci/cell µm
Xyl0.5%
WT
Δsmc
003
006
010
015
020
031
156
160
162
169
188
194
016
B
Cell length (µm)
C
WT
Sb003
Sb010
Sb021
Sb162
Sb169
Sb188
No xylose
Xylose 0.5%
Cell Density (OD 620 nm)
Time (h)

Figure S3

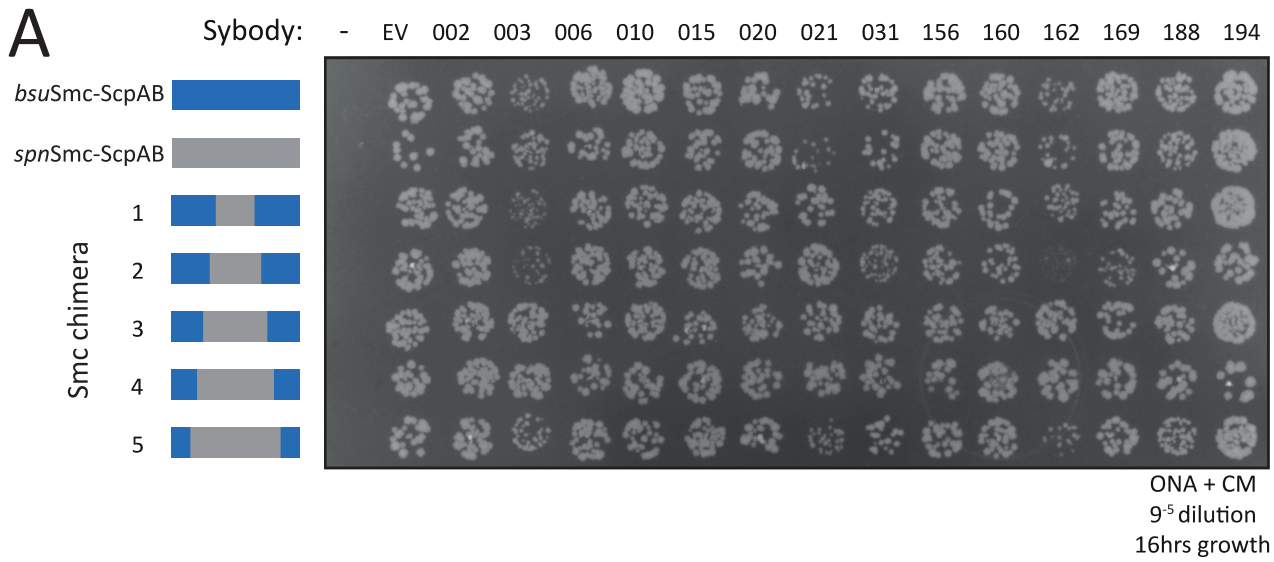
A
Sybody: - EV 002 003 006 010 015 020 021 031 156 160 162 169 188 194
bsuSmc-ScpAB
spnSmc-ScpAB
Smc chimera
1
2
3
4
5
ONA + CM
9-5 dilution
16hrs growth

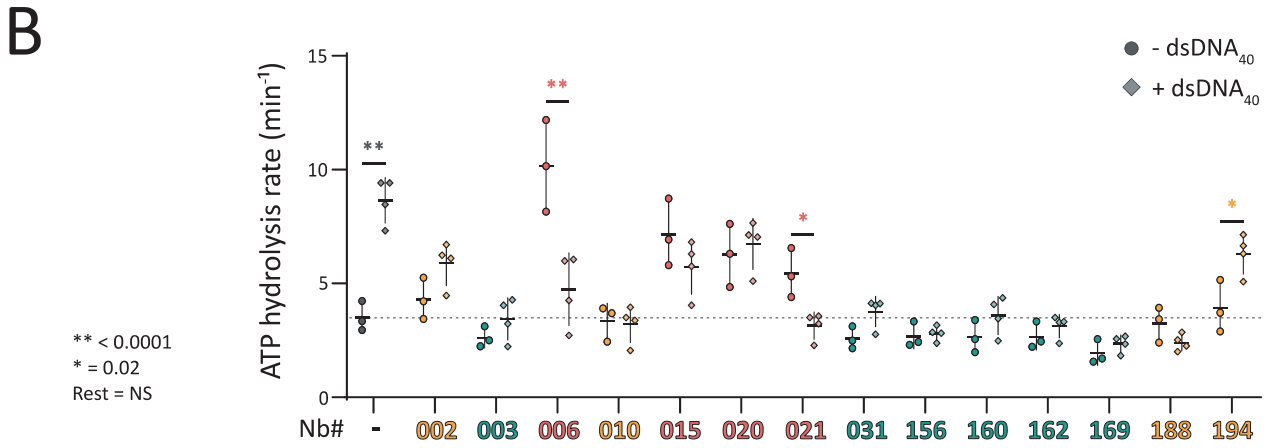
B
- dsDNA40
+ dsDNA40
ATP hydrolysis rate (min-1)
15
10
5
0
**
**
*
*
** < 0.0001
* = 0.02
Rest = NS
Nb# - 002 003 006 010 015 020 021 031 156 160 162 169 188 194

Figure S4

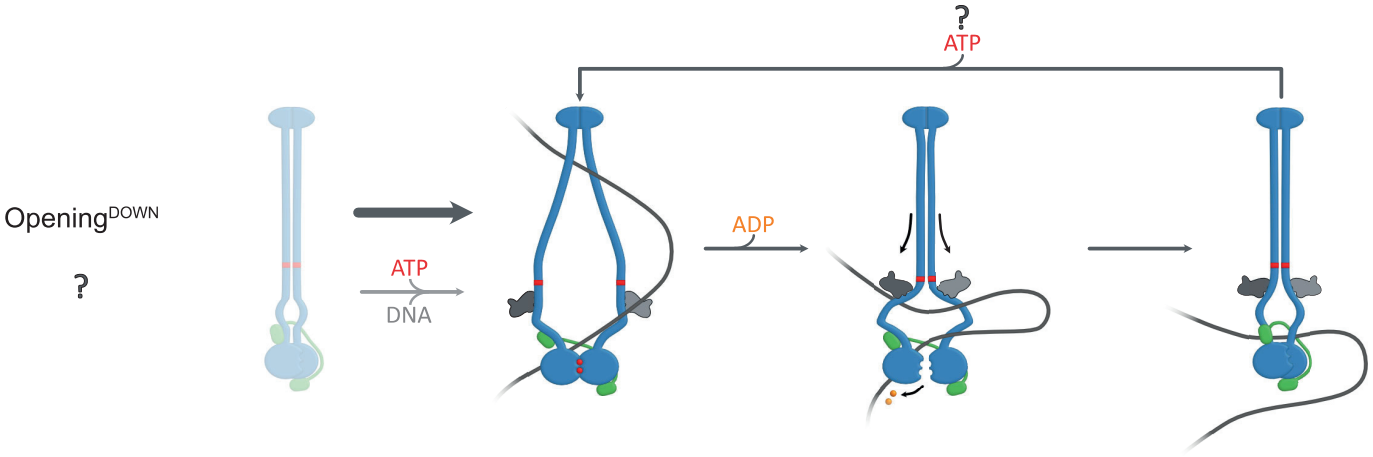

Figure S5